Infrared radiation from an extrasolar planet

Drake Deming[1], Sara Seager[3], L. Jeremy Richardson[2]
& Joseph Harrington[4]

[1]Planetary Systems Laboratory and Goddard Center for Astrobiology, Code 693;
[2]Exoplanet and Stellar Astrophysics Laboratory, Code 667, NASA's Goddard Space Flight Center, Greenbelt, Maryland 20771, USA
[3]Department of Terrestrial Magnetism, Carnegie Institution of Washington, 5241 Broad Branch Road NW, Washington DC 20015, USA
[4]Center for Radiophysics and Space Research, Cornell University, 326 Space Sciences Bldg, Ithaca, New York 14853-6801, USA

A class of extrasolar giant planets—the so-called 'hot Jupiters' (ref. 1)—orbit within 0.05 AU of their primary stars (1 AU is the Sun–Earth distance). These planets should be hot and so emit detectable infrared radiation[2]. The planet HD 209458b (refs 3, 4) is an ideal candidate for the detection and characterization of this infrared light because it is eclipsed by the star. This planet has an anomalously large radius (1.35 times that of Jupiter[5]), which may be the result of ongoing tidal dissipation[6], but this explanation requires a non-zero orbital eccentricity ($\sim$0.03; refs 6, 7), maintained by interaction with a hypothetical second planet. Here we report detection of infrared (24 μm) radiation from HD 209458b, by observing the decrement in flux during secondary eclipse, when the planet passes behind the star. The planet's 24-μm flux is 55 ± 10 μJy (1σ), with a brightness temperature of 1,130 ± 150 K, confirming the predicted heating by stellar irradiation[2,8]. The secondary eclipse occurs at the midpoint between transits of the planet in front of the star (to within ±7 min, 1σ), which means that a dynamically significant orbital eccentricity is unlikely.

Operating cryogenically in a thermally stable space environment, the Spitzer Space Telescope[9] has sufficient sensitivity to detect hot Jupiters at their predicted infrared flux levels[8]. We observed the secondary eclipse (hereafter referred to as 'the eclipse') of HD 209458b with the 24-μm channel of the Multiband Imaging Photometer for Spitzer (MIPS)[10]. Our photometric time series observations began on 6 December 2004 at 21:29 UTC (Coordinated Universal Time), and ended at approximately 03:23 UTC on 7 December 2004 (5 h 54 min duration). We analyse 1,696 of the 1,728 10-s exposures so acquired, rejecting 32 images having obvious flaws. The Supplementary Information contains a sample image, together with information on the noise properties of the data.

We first verify that circumstellar dust does not contribute significantly to the stellar flux. Summing each stellar image over a 13 × 13 pixel synthetic aperture (33 × 33 arcsec), we multiply the average sum by 1.15 to account for the far wings of the point spread function (PSF)[11], deriving a flux of 21.17 ± 0.11 mJy. The temperature of the star is close to 6,000 K (ref. 12). At a distance of 47 pc (ref. 13), a model atmosphere[14] predicts a flux of 22 mJy, agreeing with our observed flux to within an estimated $\sim$2 mJy error in absolute calibration. We conclude that the observed flux is dominated by photospheric emission, in agreement with a large Spitzer study of planet-bearing stars at this wavelength[11].

Our time series analysis is optimized for high relative precision. We extract the intensity of the star from each image using optimal photometry with a spatial weighting function[15]. Selecting the Tiny Tim[16] synthetic MIPS PSF for a 5,000-K source at 24 μm, we spline-interpolate it to 0.01 pixel spacing, rebin it to the data resolution, and centre it on the stellar image. The best centring is judged by a least-squares fit to the star, fitting to within the noise level. The best-centred PSF becomes the weighting function in deriving the stellar

photometric intensity. We subtract the average background over each image before applying the weights. MIPS data includes per-pixel error estimates[17], which we use in the optimal photometry and to compute errors for each photometric point. The optimal algorithm[15] predicts the signal-to-noise ratio (SNR) for each photometric point, and these average to 119. Our data are divided into 14 blocks, defined by pre-determined raster positions of the star on the detector. To check our SNR, we compute the internal scatter within each block. This gives SNR in the range from 95 to 120 (averaging 111), in excellent agreement with the optimal algorithm. For each point we use the most conservative possible error: either the scatter within that block or the algorithm estimate, whichever is greater. We search for correlations between the photometric intensities and small fluctuations in stellar position, but find none. We also perform simple aperture photometry on the images, and this independent procedure confirms our results, but with 60% greater errors.

The performance of MIPS at 24 μm is known to be excellent[18]. Only one instrument quirk affects our photometry. The MIPS observing sequence obtains periodic bias images, which reset the
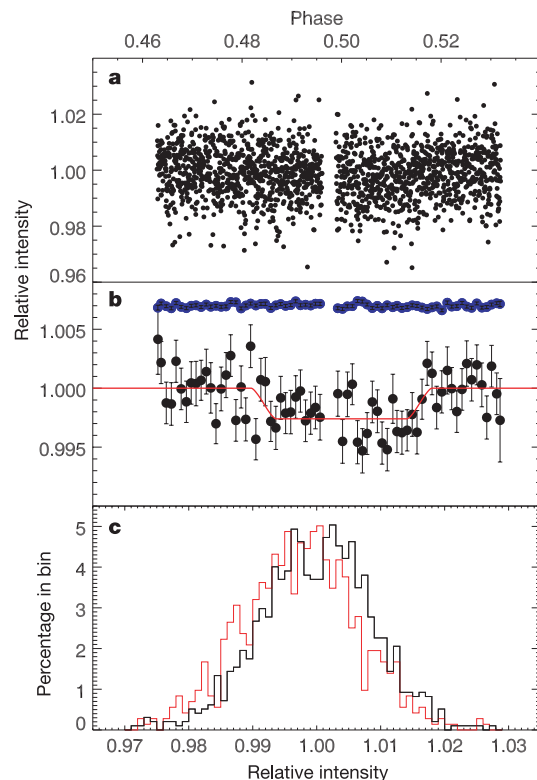

Figure 1 Observations showing our detection of the secondary eclipse in HD 209458. **a**, Relative intensities versus heliocentric phase (scale at top) for all 1,696 data points. The phase is corrected for light travel time at the orbital position of the telescope. Error bars are suppressed for clarity. The gap in the data near phase 0.497 is due to a pause for telescope overhead activity. The secondary eclipse is present, but is a factor of $\sim$4 below the $\sim$1% noise level of a single measurement. **b**, Intensities from **a**, averaged in bins of phase width 0.001 (scale at top), with 1σ error bars computed by statistical combination from the errors of individual points. The red line is the best-fit secondary eclipse curve (depth = 0.26%), constrained to a central phase of 0.5. The points in blue are a control sequence, summing intensities over a 10 × 10-pixel region of the detector, to beat down the random errors and reveal any possible systematic effects. The control sequence uses the same detector pixels, on average, as those where the star resides, but is sampled out of phase with the variations in the star's raster motion during the MIPS photometry cycle. **c**, Histograms of intensity (lower abscissa scale) for the points in **a**, with bin width 0.1%, shown separately for the out-of-eclipse (black) and in-eclipse intervals (red).

detector. Images following resets have lower overall intensities (by ~0.1–1%), which recover in later images. The change is common to all pixels in the detector, and we remove it by dividing the stellar intensities by the average zodiacal background in each image. We thereby remove variations in instrument/detector response, both known and unknown. The best available zodiacal model[19] predicts a background increase of 0.18% during the ~6 h of our photometry. Because the star will not share this increase, we remove a 0.18% linear baseline from the stellar photometry. Note that the eclipse involves both a decrease and increase in flux, and its detection is insensitive to monotonic linear baseline effects.

To detect weak signals reliably requires investigating the nature of the errors. We find that shot noise in the zodiacal background is the dominant source of error; systematic effects are undetectable after normalizing any individual pixel to the total zodiacal background. All of our results are based on analysis of the 1,696 individual photometric measurements versus heliocentric phase from a recent ephemeris[20] (Fig. 1a). We propagate the individual errors (not shown on Fig. 1a) through a transit curve fit to calculate the error on the eclipse depth. Because about half of the 1,696 points are out of eclipse, and half are in eclipse, and the SNR $\approx$ 111 per point, the error on the eclipse depth should be $\sim 0.009 \times 2^{0.5}/848^{0.5} = 0.044\%$ of the stellar continuum. Model atmospheres for hot Jupiters[2,8,21–24] predict eclipse depths in the range from 0.2–0.4% of the stellar continuum, so we anticipate a detection of 4–9σ significance. The eclipse is difficult to discern by eye on Fig. 1a, because the observed depth (0.26%) is a factor of 4 below the scatter of individual points. We use the known period (3.524 days) and radii[5] to fit an eclipse curve to the Fig. 1a data, varying only the eclipse depth, and

constraining the central phase to 0.5. This fit detects the eclipse at a depth of 0.26% $\pm$ 0.046%, with a reduced χ^2 of 0.963, denoting a good fit. Note that the 5.6σ significance applies to the aggregate result, not to individual points. The eclipse is more readily seen by eye on Fig. 1b, which presents binned data and the best-fit eclipse curve. The data are divided into many bins, so the aggregate 5.6σ significance is much less for a single bin (SNR $\approx$ 1 per point). Nevertheless, the dip in flux due to the eclipse is apparent, and the observed duration is approximately as expected. As a check, we use a control photometric sequence (Fig. 1b) to eliminate false positive detection of the eclipse due to instrument effects. We also plot the distribution of points in intensity for both the in-eclipse and out-of-eclipse phase intervals (Fig. 1c). This shows that the entire distribution shifts as expected with the eclipse, providing additional discrimination against a false positive detection.

We further illustrate the reality of the eclipse on Fig. 2. Now shifting the eclipse curve in phase, we find the best-fitting amplitude and χ^2 at each shift. This determines the best-fit central phase for the eclipse, and also further illustrates the statistical significance of the result. The thick line in Fig. 2a shows that the maximum amplitude (0.26%) is obtained at exactly phase 0.5 (which is also the minimum of χ^2). Further, we plot the eclipse 'amplitude' versus central phase using 100 sets of synthetic data, consisting of gaussian noise with dispersion matching the real data, but without an eclipse. The amplitude (0.26%) of the eclipse in the real data stands well above the statistical fluctuations in the synthetic data.

Figure 2b shows confidence intervals on the amplitude and central phase, based on the χ^2 values. The phase shift of the eclipse is quite sensitive to eccentricity (e) and is given[25] as $\Delta t = 2Pe\cos(\omega)/\pi$, where P is the orbital period, and ω is the longitude of periastron. The Doppler data alone give $e = 0.027 \pm 0.015$ (Laughlin, G., personal communication), and allow a phase shift as large as ± 0.017 (87 min). We find the eclipse centred at phase 0.5, and we checked the precision using a bootstrap Monte Carlo procedure[26]. The 1σ phase error from this method is 0.0015 (~7 min), consistent with Fig. 2b. A dynamically significant eccentricity, $e \approx 0.03$ (refs 6, 7), constrained by our 3σ limit of
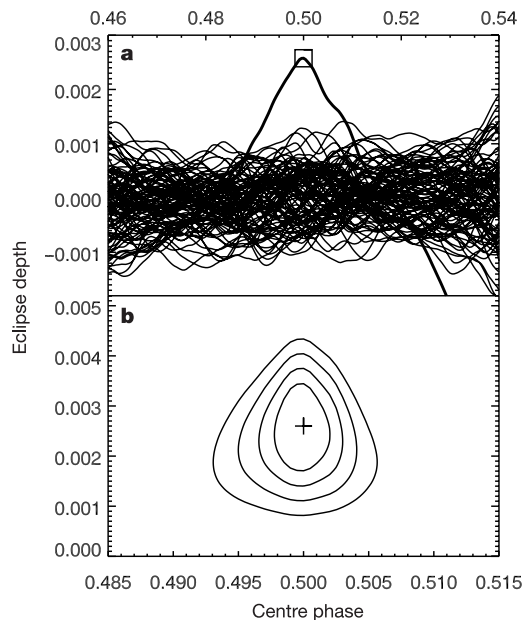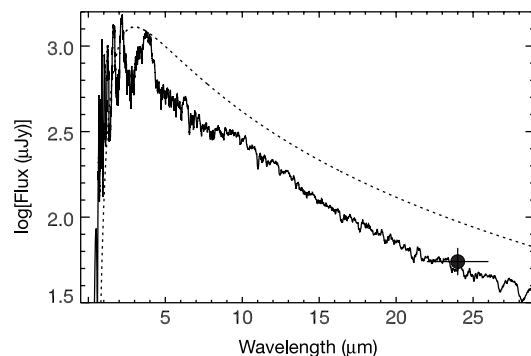

Figure 2 Amplitude of the secondary eclipse versus assumed central phase, with confidence intervals for both. **a**, The darkest line shows the amplitude of the best-fit eclipse curve versus the assumed central phase (scale at top). The overplotted point marks the fit having smallest χ^2, which also has the greatest eclipse amplitude. The numerous thinner black lines show the effect of fitting to 100 synthetic data sets containing no eclipse, but having the same per-point errors as the real data. Their fluctuations in retrieved amplitude versus phase are indicative of the error in eclipse amplitude, and are consistent with $\sigma = 0.046\%$. Note that the eclipse amplitude found in the real data (0.26%) stands well above the error envelope at phase 0.5. **b**, Confidence intervals at the 1, 2, 3 and 4σ levels for the eclipse amplitude and central phase (note expansion of phase scale, at bottom). The plotted point marks the best fit (minimum χ^2) with eclipse depth of 0.26%, and central phase indistinguishable from 0.5. The centre of the eclipse occurs in our data at Julian day 2453346.5278.

Figure 3 Flux from a model atmosphere shown in comparison to our measured infrared flux at 24 μm. A theoretical spectrum (solid line) shows that planetary emission (dominated by absorbed and re-radiated stellar radiation) should be very different from a blackbody. Hence, models are required to interpret the 24-μm flux measurement in terms of the planetary temperature. The model shown has $T_{eq} = 1,700$ K and was computed from a one-dimensional plane-parallel radiative transfer model, considering a solar system abundance of gases, no clouds, and the absorbed stellar radiation re-emitted on the day side only. Note the marked difference from a 1,700-K blackbody (dashed line), although the total flux integrated over the blackbody spectrum is equal to the total flux integrated over the model spectrum. (The peaks at short wavelength dominate the flux integral in the atmosphere model, note log scale in the ordinate.) The suppressed flux at 24 μm is due to water vapour opacity. This model lies at the hot end of the range of plausible models consistent with our measurement, but the error bars admit models with cooler T_{eq}.

$\Delta t < 21$ min, requires $|(\omega - \pi/2)| < 12$ degrees and is therefore only possible in the unlikely case that our viewing angle is closely parallel to the major axis of the orbit. A circular orbit rules out a promising explanation for the planet's anomalously large radius: tidal dissipation as an interior energy source to slow down planetary evolution and contraction[7]. Because the dynamical time for tidal decay to a circular orbit is short, this scenario posited the presence of a perturbing second planet in the system to continually force the eccentricity—a planet that is no longer necessary with a circular orbit for HD209458b.

The infrared flux from the planet follows directly from our measured stellar flux (21.2 mJy) and the eclipse depth (0.26%), giving $55 \pm 10\,\mu$Jy. The error is dominated by uncertainty in the eclipse depth. Using the planet's known radius[5] and distance[13], we obtain a brightness temperature $T_{24} = 1{,}130 \pm 150$ K, confirming heating by stellar irradiation[2]. Nevertheless, T_{24} could differ significantly from the temperature of the equivalent blackbody (T_{eq}), that is, one whose bolometric flux is the same as the planet. Without measurements at shorter wavelengths, a model atmosphere must be used to estimate T_{eq} from the 24-μm flux. One such model is shown in Fig. 3, having $T_{eq} = 1{,}700$ K. This temperature is much higher than T_{24} (1,130 K) due to strong, continuous H_2O vapour absorption at 24 μm. The bulk of the planetary thermal emission derives ultimately from re-radiated stellar irradiation, and is emitted at 1–4 μm, between H_2O bands. However, our 24-μm flux error admits a range of models, including some with a significantly lower T_{eq} (for example, but not limited to, models with reflective clouds or less H_2O vapour).

Shortly after submission of this Letter, we became aware of a similar detection for the TrES-1 transiting planet system[27] using Spitzer's Infrared Array Camera[28]. Together, these Spitzer results represent the first measurement of radiation from extrasolar planets. Additional Spitzer observations should rapidly narrow the range of acceptable models, and reveal the atmospheric structure, composition, and other characteristics of close-in extrasolar giant planets. □

1. Collier-Cameron, A. Extrasolar planets: what are hot Jupiters made of? *Astron. Geophys.* **43**, 421–425 (2002).
2. Seager, S. & Sasselov, D. D. Extrasolar giant planets under strong stellar irradiation. *Astrophys. J.* **502**, L157–L161 (1998).
3. Charbonneau, D., Brown, T. M., Latham, D. W. & Mayor, M. Detection of planetary transits across a sun-like star. *Astrophys. J.* **529**, L45–L48 (2000).
4. Henry, G. W., Marcy, G. W., Butler, R. P. & Vogt, S. S. A transiting "51 Peg-like" planet. *Astrophys. J.* **529**, L41–L44 (2000).
5. Brown, T. M., Charbonneau, D., Gilliland, R. L., Noyes, R. W. & Burrows, A. Hubble Space Telescope time-series photometry of the transiting planet of HD 209458. *Astrophys. J.* **552**, 699–709 (2001).
6. Bodenheimer, P., Lin, D. N. C. & Mardling, R. A. On the tidal inflation of short-period extrasolar planets. *Astrophys. J.* **548**, 466–472 (2001).
7. Laughlin, G. *et al.* A comparison of observationally determined radii with theoretical radius predictions for short-period transiting extrasolar planets. *Astrophys. J.* (in the press).
8. Burrows, A., Sudarsky, D. & Hubeny, I. in *The Search for Other Worlds: Proc. 14th Annu. Astrophys. Conf. in Maryland* (eds Holt, S. & Deming, D.) Vol. 713, 143–150 (American Institute of Physics, Melville, New York, 2003).
9. Werner, M. W. *et al.* The Spitzer Space Telescope mission. *Astrophys. J. Suppl.* **154**, 1–9 (2004).
10. Rieke, G. H. *et al.* The Multiband Imaging Photometer for Spitzer (MIPS). *Astrophys. J. Suppl.* **154**, 25–29 (2004).
11. Beichman, C. A. *et al.* Planets and IR excesses: preliminary results from a *Spitzer* MIPS survey of solar-type stars. *Astrophys. J.* (in the press).
12. Ribas, A. H., Solano, E., Masana, E. & Gimenez, A. Effective temperatures and radii of planet-hosting stars from IR photometry. *Astron. Astrophys.* **411**, L501–L504 (2003).
13. Perryman, M. A. C. (ed.) *The Hipparcos and Tycho Catalogues* (ESA SP-1200, European Space Agency, Noordwijk, 1997).
14. Kurucz, R. *Solar Abundance Model Atmospheres for 0, 1, 2, 4, and 8 km/s* CD-ROM 19 (Smithsonian Astrophysical Observatory, Cambridge, Massachusetts, 1994).
15. Horne, K. An optimal extraction algorithm for CCD spectroscopy. *Publ. Astron. Soc. Pacif.* **98**, 609–617 (1986).
16. Krist, J. in *Astronomical Data Analysis Software and Systems IV* (eds Shaw, R. A., Payne, H. E. & Hayes, J. J. E.) Vol. 77, 349–352 (Astronomical Society of the Pacific, San Francisco, 1995).
17. Gordon, K. D. Reduction algorithms for the Multiband Imaging Photometer for SIRTF. *Publ. Astron. Soc. Pacif.* (in the press).
18. Rieke, G. H. *et al.* in *Proc. SPIE: Optical, Infrared, and Millimeter Space Telescopes* (ed. Mather, J. C.) Vol. 5487, 50–61 (SPIE, Bellingham, Washington, 2004).
19. Kelsall, T. *et al.* The COBE Diffuse Infrared Background Experiment (DIRBE) search for the cosmic infrared background. II. Model of the interplanetary dust cloud. *Astrophys. J.* **508**, 44–73 (1998).
20. Wittenmyer, R. A. *The Orbital Ephemeris of HD 209458b.* Master's thesis, San Diego State Univ. (2003).
21. Goukenleuque, C., Bezard, B., Joguet, B., Lellouch, E. & Freedman, R. A radiative equilibrium model of 51 Peg b. *Icarus* **143**, 308–323 (2000).
22. Seager, S., Whitney, B. A. & Sasselov, D. D. Photometric light curves and polarization of close-in extrasolar giant planets. *Astrophys. J.* **540**, 504–520 (2000).
23. Barman, T. S., Hauschildt, P. H. & Allard, F. Irradiated planets. *Astrophys. J.* **556**, 885–895 (2001).
24. Sudarsky, D., Burrows, A. & Hubeny, I. Theoretical spectra and atmospheres of extrasolar giant planets. *Astrophys. J.* **588**, 1121–1148 (2003).
25. Charbonneau, D. in *Scientific Frontiers in Research on Extrasolar Planets* (eds Deming, D. & Seager, S.) Vol. 294, 449–456 (Astronomical Society of the Pacific, San Francisco, 2003).
26. Press, W. H., Teukolsky, S. A., Vettering, W. T. & Flannery, B. P. *Numerical recipes in C* 2nd edn (Cambridge Univ. Press, Cambridge, 1992).
27. Alonso, R. *et al.* TrES-1, the transiting planet of a bright K0V star. *Astrophys. J.* **613**, L153–L156 (2004).
28. Charbonneau, D. *et al.* Detection of thermal emission from an extrasolar planet. *Astrophys. J.* (in the press).